V.U. Mr. Michel Sonck ISSN - 0250 - 5010

ANNALEN
VAN
DE BELGISCHE VERENIGING
VOOR
STRALINGSBESCHERMING

VOL. 47-1, 2023

Radiation Effects on Materials

ANNALES
DE
L'ASSOCIATION BELGE
DE
RADIOPROTECTION

V.U. Mr. Michel Sonck ISSN - 0250 - 5010

ANNALEN
VAN
DE BELGISCHE VERENIGING
VOOR
STRALINGSBESCHERMING

VOL. 47-1, 2023

Radiation Effects on Materials

ANNALES
DE
L'ASSOCIATION BELGE
DE
RADIOPROTECTION

Annales de l'Association belge de Radioprotection (BVSABR)

Annalen van de Belgische Vereniging voor Stralingsbescherming (BVSABR)

Vol. 47-1/2023

Radiation Effects on Materials

The Belgian Society for Radiation Protection organised in 2020 a scientific meeting on the Surveillance of Radioactivity un the Environment.

This publication compiles two texts that were provided by lecturers who made presentations at the meeting.

The BVSABR

Redaction Committee

Annales de l'Association belge de Radioprotection (BVSABR)

Annalen van de Belgische Vereniging voor Stralingsbescherming (BVSABR)

Vol. 47-1/2023

Radiation Effects on Materials

CONTENT

The influence of irradiation on reactor pressure vessel materials

Evy De Bruycker[1], Robert Gérard[2], Rachid Chaouadi[3]

[1] ENGIE Laborelec, Rodestraat 125, B-1630 Linkebeek
[2] Tractebel Engineering, Boulevard Simon Bolivar 34–36, B-1000 Brussel
[3] SCK CEN, Boeretang 200, B-2400 Mol

Abstract

In most industrial applications metallic materials will age over time, leading to a gradual deterioration of their mechanical properties. For Reactor Pressure Vessel (RPV) steels, apart from time and temperature, also irradiation will play a role in this ageing process.

This paper will explain some of the mechanisms that take place inside the material due to irradiation, causing embrittlement. The corresponding consequences on the mechanical properties will be discussed, as well as the methodology that is used by ENGIE to predict and follow up this gradual ageing for the Belgium nuclear power plants.

Keywords: material ageing, radiation damage, RPV steel

Introduction

Nuclear safety is critical to the operation of any nuclear component, and the reactor pressure vessel (RPV) is probably the most critical component for which safe operation should be guaranteed at any time and in all conditions, including accidental conditions. Although many other components can be replaced, this operation would be extremely complex (if at all feasible) for the RPV, which is generally considered as irreplaceable, and therefore can limit the lifetime of a nuclear power plant.

The RPV is made out of carbon steel, which experiences irradiation embrittlement over time due to neutron irradiation. Hence, it is important to properly monitor the evolution of the properties of the RPV material under operating conditions, by means of a surveillance program.

This paper explains the mechanisms of irradiation embrittlement, the corresponding influence on the mechanical properties of the material and the main principles of the surveillance program.

Mechanism of Irradiation ageing

In materials subject to neutron irradiation, neutrons hit lattice-atoms, called primary knock-on atoms (PKAs). If the transferred energy in such a collision is higher than the displacement threshold energy, the PKA leaves its site and starts moving through the lattice. The initial kinetic energy of the PKA is called 'recoil energy' [1]**.**

During its displacement, a PKA may be slowed down by interactions with electrons and/or collisions with other atoms, called secondary knock-on atoms (SKAs). These SKAs can also leave their site and then be slowed down by the same mechanisms; the tertiary knock-on atoms can proceed in the same way and so on. This process results in a series of atomic displacements designated a 'displacement cascade'. This phase takes a fraction of a picosecond.

Once all the PKA energy is dissipated through such interactions, most of the created vacancies and self-interstitial atoms (SIAs) annihilate each other. At the end of this recombination phase (which lasts a few picoseconds), only some point defects survive. The whole process is called primary damage.

The primage damage shows two main phases:

- A ballistic (or collision) phase lasting a few tenths of a picosecond. During this phase, the energy of the PKA is distributed by multiple collisions among atoms, with the result that they leave their lattice sites. This creates a central disordered core surrounded by a mantle of SIAs.
- A recombination phase during which most of the SIAs in the outer mantle return to lattice sites by non-thermal relaxation. This phase lasts some picoseconds. The non-recombined SIAs and vacancies constitute the so-called "surviving defects".

Displacement cascades cannot be studied experimentally, due to their short lifetime (some picoseconds) and small space extension (some nanometres). Therefore, since the 1960s strong efforts have been devoted to their simulation.

The atomic rearrangements produced by displacement cascades give a weak contribution to the evolution of the properties of irradiated RPV steels. It is the migration of some of the surviving point defects that is responsible for such evolution. As a result of the primary damage, vacancies and SIAs are in excess. The excess vacancy concentration will induce radiation-enhanced diffusion (RED) and the formation of irradiation-induced defects (secondary defects). These defects evolve in time as a function of the vacancy generation (irradiation conditions) and the available elements still present in the matrix.

There are two families of irradiation-induced defects: precipitates and so-called stable matrix features (SMFs), made of SIAs, vacancies and solute atoms (other large atoms that take the place of Fe atoms in the steel lattice) [1]. Table 1 provides a classification of these defects as well as some of their characteristics, evaluated from experimental or simulation work.

Table 1: irradiation-induced defects in RPV steels [1].

Type		Size (nm)	Number density (m^{-3})	Composition
Precipitates	CRPs	0.5-1.5	Some 10^{24}	Cu (>50%)-Mn-Ni-Si
	MNPs	0.5-1.5	Some 10^{24}	Mn-Ni-Si (>50%)-Cu
SMFs	Dilute solute atmospheres	< 2nm	< 10^{24}	Fe-Cu-Mn-Ni-Si
	Vacancy-solute clusters	< 0.5-1.5nm	< 10^{24}	Vacancies -Cu-Mn-Ni-Si
	Nanovoids	< 0.5nm	< 10^{24}	Vacancies -Cu-Mn-Ni-Si
	SIA clusters	< 0.3nm	Some 10^{24}	-
	SIA dislocation loops	< 0.8nm	Some 10^{24}	-

Impact of irradiation on material properties

Irradiation-induced defects constitute obstacles to the gliding of dislocations and hence harden RPV steels. This is called hardening embrittlement. Dislocations can pass through the smallest defects (only a few atoms in size or point defects) by thermally activated mechanisms and, therefore these defects, have no hardening effect at room temperature; the other defects are passed by non-thermal mechanisms and thus control the hardening in a wide range of temperatures [1].

In the absence of intergranular rupture, the RPV steel response to neutron irradiation can be described as an irradiation-induced increase in yield strength, which in turn reduces the ductility and the fracture toughness. Below a certain temperature a carbon steel becomes brittle. This temperature is called the Ductile to Brittle Transition Temperature (DBTT). Irradiation will cause a shift in this DBTT to a higher temperature. In a wide range of temperatures, the irradiation-

induced hardening of RPV steel is mainly controlled by non-thermal mechanisms and hence is independent of the testing temperature. This independence, together with the steep temperature dependence of the yield strength typical of bcc structure, provides a qualitative explanation for the irradiation-induced shift of the DBTT, as illustrated in Figure 1.

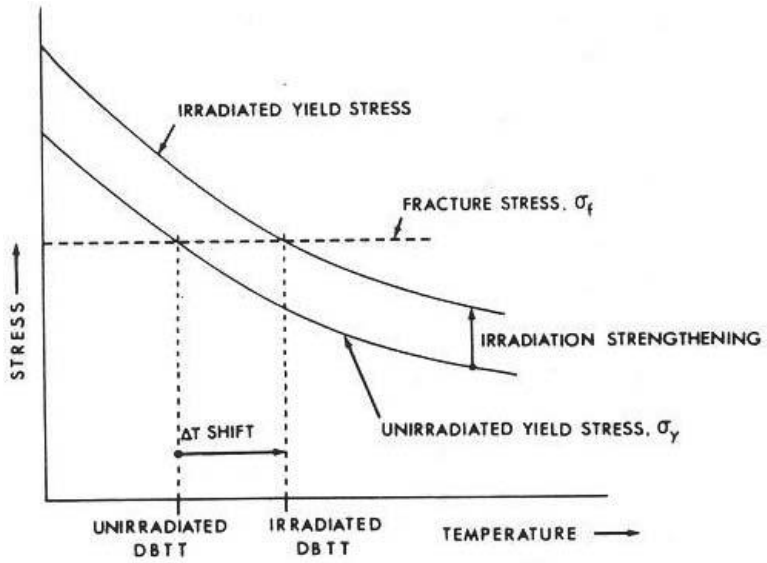

Figure 1: Schematic diagram showing how an irradiation-induced increase of yield stress results in a DBTT shift [1].

In some cases, irradiation embrittlement can occur without the corresponding increase in yield strength. This is called non-hardening embrittlement. The main mechanism for this non-hardening embrittlement is the segregation of impurities (like P) to the grain boundaries, promoting intergranular fracture.

Prediction and follow-up of irradiation ageing [2]

Reactor pressure vessel irradiation embrittlement is monitored by means of surveillance capsules containing samples from a cut-out ring of the core shells that make up the RPV that are inserted in the RPV before the start of operation.

These capsules are placed at locations in which they receive a higher neutron flux than the vessel wall, by a factor of the order of two to three. They are regularly retrieved and tested to evaluate RPV irradiation embrittlement according to specific regulatory procedures and standards to guarantee the safe operation of the RPV throughout its lifetime. These procedures often rely on empirical but conservative concepts.

The classical surveillance approach is based largely on the Charpy impact tests (standardized high strain rate test which determines the amount of energy absorbed by a material during fracture). The key property that is used for the assessment of RPV integrity is the ductile-to-brittle transition temperature (DBTT). The procedures that were developed within the ASME code [3] are essentially empirical and rely on a number of correlations.

Embrittlement trend curves are used to predict RPV embrittlement on the basis of the chemical composition and fast neutron fluence (E > 1 MeV). The surveillance results are systematically compared to these trend curves to confirm that their predictions are conservative (Figure 2).

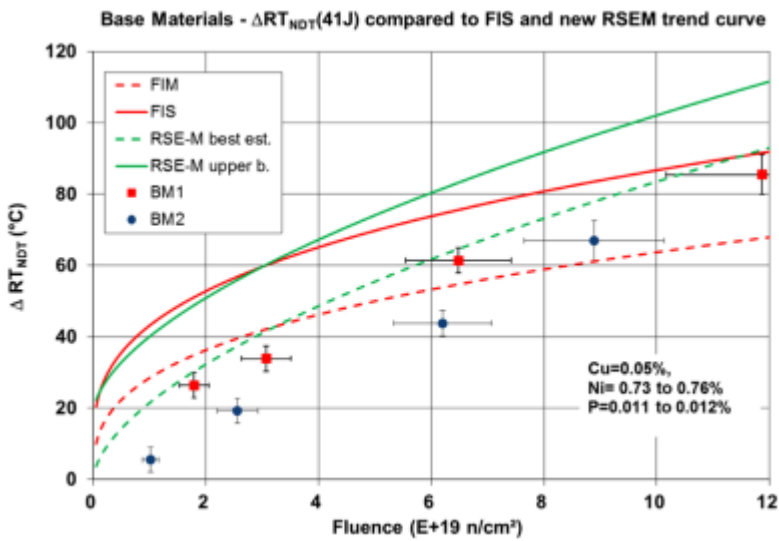

Figure 2: Example of surveillance results compared to trend curves. FIM, FIS and RSE-M are different types of trend curves. BM=base material.

Taking advantage of the improved understanding of irradiation effects, analytical tools have been developed to improve the quality of RPV embrittlement assessment. These tools become particularly important in case of operation beyond the original design life of 40 years. In this framework, a complementary and enhanced, surveillance program assessment has been developed in Belgium, which benefits from the latest developments in the area of material science and irradiation effects.

This enhanced surveillance has been systematically applied for 15 years in the evaluation of the surveillance programs of the Belgian units, to provide additional insight and reliability of the data. In the enhanced surveillance strategy, five pillars can be identified:

- Specimen reconstitution: This technology allows fabricating additional specimens from fractured Charpy samples that can be tested according to the most recent standards and evaluation procedures (
- Figure ***3***).[1]
- Fracture mechanics: The reconstituted Charpy specimens offer the possibility of performing fracture toughness tests. It is now possible to perform valid fracture toughness tests on small specimens thanks to the specimen size correction introduced in the Master Curve approach [4].
- Load diagram analysis: The Charpy impact test data together with the tensile data can be analysed in a consistent and unique manner to better assess the measured irradiation-induced embrittlement [2].
- Damage modelling: An engineering physically based hardening model was developed at SCK CEN [5] that allows rationalizing all available data either to evaluate similar materials or when investigating other irradiation conditions [6].
- Microstructure: Whenever required, it is important to visualize and evaluate the irradiation-induced defects with the most advanced

[1] ASTM E1253, Standard Guide for Reconstitution of Irradiated Charpy-Sized Specimens, is available for performing Charpy-sized reconstitution. The reconstitution technology is currently well established and has been the subject of many publications in the past, e.g., the European project RESQUE was devoted to this topic. [8]

techniques such as atom probe tomography, small-angle neutron scattering and positron annihilation spectroscopy.

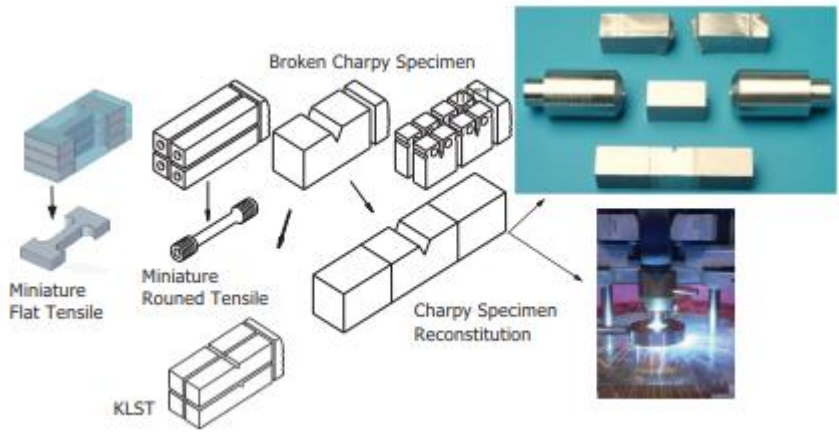

Figure 3: Example of specimen reconstitution: Charpy-sized, KLST (mini-Charpys), and miniature tensile and compact tensile (mCT) specimens [5].

The enhanced surveillance approach complements the mandatory regulatory procedure, which remains the basis of the justification of the safe operation of the RPV's, but provides an increased confidence in the results and allows quantifying the conservatism of the regulatory approach. Using the reconstitution technology to fabricate additional small-sized specimens, appropriate modelling tools and microstructural examination if required, it is possible to rationalize in a physical way all available information and to increase the reliability of the integrity assessment of the RPV.

References

[1] IAEA, “Integrity of reactor pressure vessels in nuclear power plants: assessment of irradiation embrittlement effects in reactor pressure vessel steels,” 2009.

[2] R. Gérard and R. Chaouadi, “Reactor pressure vessel surveillance programs in Belgium,” in *International Review of Nuclear Reactor Pressure Vessel Surveillance Programs*, West Conshohocken, PA, ASTM STP1603, 2018, pp. 250-275.

[3] ASME, “Test Requirements and Acceptance Standards,” ASME Code, Section II, Division 1, Article NB-2330, New-York, 1992.

[4] ASTM E1921, “Standard test method for determination of reference temperature, T0, for ferritic steels in the transition range,” ASTM International, West Conshohocken, PA, 2012.

[5] R. Chaouadi, “An engineering radiation hardening model of reactor pressure vessel materials,” SCK-CEN, R-4235, 2005.

[6] R. Gérard, R. Chaouadi and D. Bertolis, “Neutron flux effect on the fracture toughness behavior of Tihange-III RPV material,” in *Fontevraud 8*, Avignon, France, 2014.

[7] R. Gérad and R. Chauoadi, “An effective surveillance strategy for reactor pressure vessel assessment in the long term operation perspective,” in *Fontevraud 8*, Avignon, France, 2014.

[8] E. van Walle, M. Scibetta, M. Valo, H.-W. Viehrig, H. Richter, T. Atkins, M. Wootom, E. Keim, L. Debarberis and M. Horsten, "RESQUE: Reconstitution Techniques Qualification and Evaluation to Study Ageing Phenomena of Nuclear Pressure Vessel Materials," in *Small Specimen Test Techniques, ASTM STP1418*, West Conshohocken, PA, ASTM International, 2022, pp. 409-425.

The effect of gamma irradiation on $CaO\text{-}Fe_xO_y\text{-}SiO_2$ slag-based inorganic polymers

Bram Mast[1], Alexios P. Douvalis[2], Isabelle Gerardy[3], Grazyna Gryglewicz[4], Yiannis Pontikes[5], Wouter Schroeyers[1], Bram Vandoren[6], Sonja Schreurs[1**]*

[1] *Hasselt University, CMK, NuTeC, Nuclear Technology - Faculty of Engineering Technology, Agoralaan Building H, B-3590 Diepenbeek, Belgium*

[2] *University of Ioannina, Department of Physics, 45110 Ioannina, Greece*

[3] *Haute Ecole Bruxelles-Brabant HE2B, ISIB, Engineering Education Institute, Physical and Nuclear Department, Koningsstraat 150, B-1000 Brussels, Belgium*

[4] *Wrocław University of Science and Technology, Faculty of Chemistry, Department of Polymer and Carbonaceous Materials, Gdańska 7/9, 50-344 Wrocław, Poland*

[5] *KU Leuven, Department of Materials Engineering, Kasteelpark Arenberg 44, 3001 Heverlee, Belgium*

[6] *Hasselt University, CERG, Faculty of Engineering Technology, Agoralaan Building H, B-3590 Diepenbeek, Belgium*

[*] *Main Author, E-mail: bram.mast@uhasselt.be*

[**] *Corresponding Author: sonja.schreurs@uhasselt.be*

Abstract

Cementitious materials, other than the commonly used ordinary Portland cement, are increasingly being studied for the encapsulation of radioactive waste. In this respect geopolymers and inorganic polymers (IPs) have received broad attention. The absence of portlandite, their low water content and high alkalinity make IPs interesting candidates for the conditioning of certain radioactive waste streams. Moreover, Fe-rich IPs offer an interesting alternative to high-density concretes in radiation shielding applications. Materials can however be altered by exposure to ionizing radiation, hence the need to study the material's behaviour under irradiation conditions. This study investigates the effect of gamma irradiation on IPs based on $CaO\text{-}Fe_xO_y\text{-}SiO_2$ slag. Samples with different curing times prior to irradiation (1 h, 24 h and 28 days) were irradiated at different dose rates varying from 1.52 Gy/h to 8.85 kGy/h and doses varying from 137 Gy to 715 kGy. Non-irradiated samples were kept as a reference, in the same environmental condition as for each irradiated sample.

The effects of gamma irradiation are observed to be very dependent on the curing time prior to irradiation. The mechanisms leading to the irradiation effects are different for non-hardened samples and for hardened samples. Multiple effects were observed: a change in macroscopic strength, a change in porosity, radiation-altered carbonation, a decrease in water content and an increase in the $Fe^{3+}/\Sigma Fe$ ratio.

Keywords: inorganic polymers (IP), radiation effects, curing time

Introduction

Alternatives to the commonly used ordinary Portland cement (OPC) matrices are, for a number of decades, increasingly being studied for radioactive waste encapsulation. Inorganic Polymers (IPs) are among the alternatives currently being studied. IPs encompass a broad range of binder systems formed by the reaction of an alkali metal source with a solid amorphous powdered precursor [1]. A three-dimensional-tetrahedral network is formed in which the aluminates and silicates are covalently bonded by shared oxygen atoms [2]. The alkali source can be any solid or solution that can raise the pH of the reaction mixture and dissolve the precursor [1].

The chemistry of alkali-activation can be summarized in four steps: (i) dissolution, (ii) reorganization, (iii) nucleation and (iv) polymerization and hardening [3]. In the first step, the ionic and covalent bonds are broken at the surface of the precursor material in contact with the high alkaline solution. Next, the diffusion of the alkali solution will bring more Al^{3+} and Si^{4+} into solution. In the alkaline environment the alumina and silica form monomeric tetrahedral structures of $Al(OH)_4^-$ and $Si(OH)_4$. Due to polycondensation reactions, the gel will harden by the formation of an amorphous 3D network of Al-O-Si chains. In this structure, each Al- and Si-atom is bound to four oxygen atoms. The resulting negative charge is compensated by the cations present in the activation solution (e.g. Na^+, K^+, Li^+, Ca^{2+}, Ba^{2+}, NH_4^+, H_3O^+). Moreover, a recent study by Peys et al. [4] indicates the participation of iron in the silicate network, which enables the use of Fe-rich precursors for IP production. Slags originating from nonferrous metallurgical industries, which are currently underutilized can thus be used as a precursor for IP production [4]. While the process is summarized in four steps, it should be emphasized that the steps occur simultaneously [5] [6]. At the end, a three-phase material is formed consisting of pores, binder and aggregates, the binder consisting of reacted precursor material and the aggregates of non-reacted precursor particles (Figure 4).

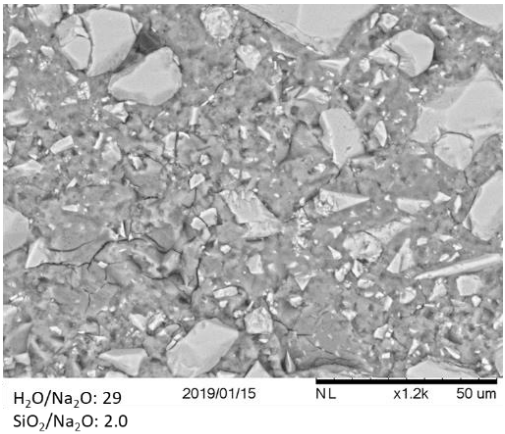

Figure 4: SEM image of a plasma slag based AAM.

Alkali activation technology is recognized to have a high potential for immobilization of hazardous components [7] [8]. Due to the wide range of available precursors and activation solutions, tailor-made alkali activated materials (AAMs) can be designed for certain applications. The high pH of the AAMs insolubilizes many metals and radioelements such as ^{137}Cs, and protects steel from corrosion [9] [10] [11].

On the other hand, the high alkalinity of the AAMs favours the corrosion of reactive metals, leading to additional hydrogen formation. In this case, low-alkaline AAMs need to be designed. AAMs also have a high chemical and temperature resistance [2] [12] and can be designed to have a low water content. This limits the radiolytic hydrogen production and avoids freeze-thaw problems. AAMs moreover have a high radionuclide retention capacity due to the absence of portlandite ($Ca(OH)_2$), which has a weak immobilization potential, due to their low porosity and low critical pore diameter [25]–[27].

Several immobilization mechanisms have been reported in the literature: (i) AAMs can immobilize cations (e.g. Cs^+) as a charge-balancing ion replacing Na^+ or K^+ [28] [29], (ii) cations (e.g. Sr^{2+}) can be incorporated in C-S-H phase replacing Ca^{2+} [30] [31], (iii) ions can directly be incorporated in (N(-C)-A-S(-H) aluminosilicate structures [11] [17] [19] [20] [32] [33] and (iv) radionuclides can be adsorbed on introduced or self-generated zeolite structures [31] [34]–[36].

IPs based on slags are very promising for use as gamma shielding material. High linear attenuation coefficients can be obtained using cheap slags, avoiding the expensive aggregates currently used to produce high density concretes [14]. IPs based on fayalite slags were proven to have a similar gamma shielding capacity as basalt-magnetite concretes [14]. Also for neutron shielding IPs offer an interesting opportunity since boron can be incorporated in the matrix to substitute aluminium [15]. Moreover, IPs dehydrate less with time in comparison with fresh OPC samples, which allows to easily design IPs with better neutron shielding capacities compared to aged concrete [16].

However, these beneficial properties do not ensure that an AAM binder formulation is suitable for conditioning a particular radioactive waste stream. An example in which the use of AAMs is better than OPC-based binders is the immobilization of reactive metals such as Mg-Zr alloys. Since AAMs have a low amount of Ca [37], NaF can be added to decrease H_2 production resulting from Mg corrosion. In Ca-rich binders, a CaF_2 precipitate is formed which in addition deteriorates the mechanical properties. AAMs also have the advantage of a high amount of silicates that can form a layer of $MgSiO_4$ on the surface of the magnesium, preventing it from corrosion [38] [39] and thus limiting H_2 production.

This work focusses on the effects of gamma irradiation on inorganic polymers. The effect of gamma irradiation is investigated on IPs based on iron-rich CaO-Fe_xO_y-SiO_2 slag.

Material and Methods

In our study plasma slag was chosen as resource material for the IP production. This slag is the end product of the gasification of municipal solid waste. Plasma slag belongs to a large group of non-ferrous metallurgy residues with a high iron content. When the slag is cooled rapidly the resulting granulates are highly amorphous [40], making it a good candidate for IP production.

A synthetic plasma slag was produced using urban solid waste incinerated bottom ash, iron ore, limestone and sand to create an ash with a similar composition to enhanced landfill mining ash. The glass was milled using a ball mill until reaching, before alkali activation, a Blaine value of $(2.68 \pm 0.02)\ 10^3$

cm²/g (according to EN 196-6 [41]). The chemical composition of the synthetic plasma slag was determined using X-ray fluorescence analysis (Bruker AXS S8 TIGER spectrometer). High amounts of SiO_2, Fe_xO_y, CaO and Al_2O_3 were detected (Table 2).

Table 2: Chemical composition of synthetic plasma slag (PS) according to XRF.

wt.%	SiO_2	Fe_xO_y	CaO	Al_2O_3	MgO	TiO_2	K_2O	Na_2O	CuO	MnO
PS	29.2	28.2*	26.7	13.4	0.8	0.7	0.6	0.2	0.1	0.1

*expressed as 92 % FeO and 8 % Fe_2O_3

The IPs were produced by mixing the dry milled slag with a sodium silicate activation solution in a solid to liquid ratio of 2.6 kg/l. The solution was a mixture of sodium silicate, sodium hydroxide pellets and distilled water (SiO_2/Na_2O molar ratio = 1.6 and H_2O/Na_2O molar ratio =20.0)[2].

Samples cured for 1 h, 24 h or 28 d prior to irradiation were tested. These time intervals were chosen on the basis of the different reaction stages:

- 1 h: minimum time after casing necessary to load the samples in the irradiation cell
- 24 h: right after the main reaction peak
- 28 d: stable and fully cured sample.

The different curing times correspond to different material applications in radioactive waste management. For certain barriers prefabricated and fully hardened materials are preferred, while for others the material is poured close to the radioactive source(s), causing irradiation during hardening.

Different **irradiation experiments** were performed as summarized in Table 3.

[2] This recipe has only been used in experiment D. For the other experiments a different mix has been used.

Table 3: Description of the four different irradiation experiments.

	A	B	C	D
	Low dose rate	**Intermediate dose rate**	**High dose rate**	**Very High dose rate**
Location	HE^{2}B ISIB	UHasselt	HE^{2}B ISIB	SCK CEN
Source	^{60}Co	^{137}Cs	^{137}Cs	^{60}Co
Energy	1.173 MeV & 1.332 MeV	0.662 MeV	0.662 MeV	1.173 MeV & 1.332 MeV
Activity	~1 TBq	35 TBq	123 TBq	unknown
Max dose rate	6.9 ± 0.15 Gy/h 1.52 ± 0.03 Gy/h	152 ± 8 Gy/h	1.25 kGy/h	8.85 kGy/h
Dose interval	0.032 kGy – 47 kGy	0.152 kGy – 95 kGy	3 kGy - 390 kGy	200 kGy
Time before irradiation	24 h or 28 d	1 h	24 h	1 h, 24 h or 28 d
Charac-terization	Immediately after irradiation	at 28 d of hardening. After irradiation, the samples were placed in a curing chamber	Immediately after irradiation	Immediately after irradiation

Reference samples identical to the irradiated ones were used for each irradiation test. Except for the irradiation, the same procedures were applied to both:

- **Macro-mechanical strength**

  Uniaxial compressive strength tests were performed on samples of (25 x 25 x 20) mm³ according to NBN EN 12390-3 using the Instron 5985 at a displacement of 1.0 mm/min.

- **Mercury Intrusion Porosimetry**

  MIP was performed using the Micromeritics Autopore IV 9510. Samples of (5 x 5 x 5) mm^3 were used. The samples were tested in the range of 0.01 to 414 MPa, applicable to quantify pores in the 3.6 nm to 100 µm region.

- **Attenuated Total Reflectance Fourier-transformed infrared**

  A Bruker Alpha-P with diamond crystal was used on powdered samples. 32 spectra per sample were acquired from 4000 cm^{-1} to 380 cm^{-1} at a resolution of 4 cm^{-1}. The reported spectra are the result of an average of five measurements.

- **Thermogravimetric analysis**

  TGA (TGA 550 - TA instruments) of the powdered samples was carried out from 20 °C to 1000 °C with a heating rate of 10 °C/min in a nitrogen atmosphere. The mass was measured with 10^{-6} g precision.

- **^{57}Fe Mössbauer spectroscopy**

  Samples were powdered manually and pressed into the sample holder right before measurement. Gamma rays from a ^{57}Co source in a Rh matrix were used. The samples were measured at room temperature (RT, 300 K) in transmission geometry on a constant acceleration spectrometer. The isomer shift (IS) values are reported relative to α-Fe at RT. The IMSG software was used to fit the data [42].

Results and Discussion

Figure 5 summarises the results of all compressive strength tests executed for the different irradiation experiments. The relative strength change is predominantly positive above 5 kGy and increases further with increasing absorbed dose. Below 5 kGy on the other hand, mainly a negative impact on the strength is observed. This suggests two opposing effects: at low dose rates and low absorbed doses the detrimental effects on strength predominate, for high doses (> 5 kGy) the beneficial effects. The effects are the strongest for IP samples cured for only 1 h prior to irradiation (+). For the 28 d cured samples (■) on the other hand, the

effects stay within the -16 % and +18 % limits, with one exception at +55 %.

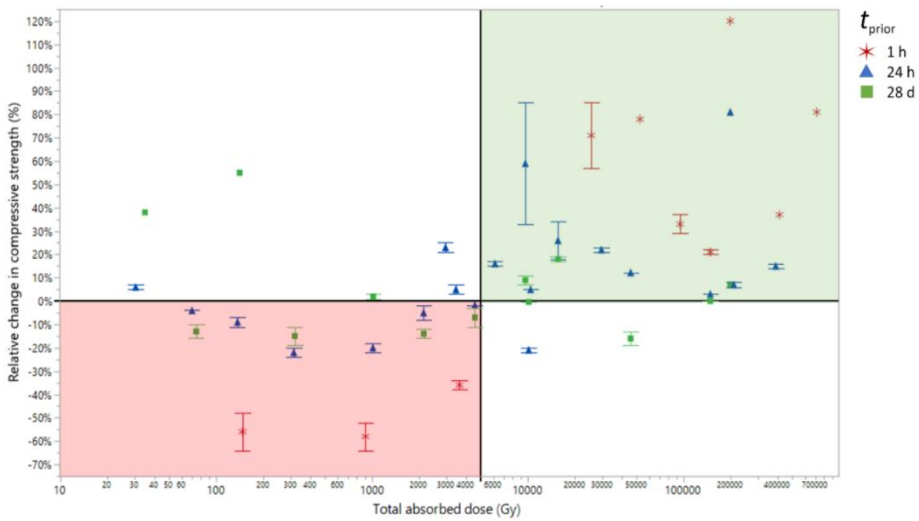

Figure 5: Overview of change in compressive strength relative to the corresponding reference with one standard error of the mean, in function of the total absorbed dose for all the executed experiments.

The samples irradiated at 8.85 kGy/h (D) to a total dose of 200 kGy showed in increase in strength by a factor 2.2 and a factor 1.81 for samples with t_{prior}= 1 h and t_{prior}= 24 h, respectively. For the 28 d cured samples, no significant difference was observed as a result of irradiation. In this document, the focus will be on the results of irradiation experiment D with samples cured for a time t_{prior} = 1 h. More results and details can be found in other related publications [43] [44].

The porosity and pore size distribution (PSD) of irradiated and non-irradiated samples were determined using MIP analysis (Figure 6). The size diameter of the pores is mainly in the range 100 - 2000 nm and in the range < 10 nm. The porosity of the 1 hour cured samples was significantly reduced in the 100 - 2000 nm region as a result of irradiation, with a shift to the smaller pore sizes. For pores smaller than 10 nm a small shift to larger pore size diameters was detected.

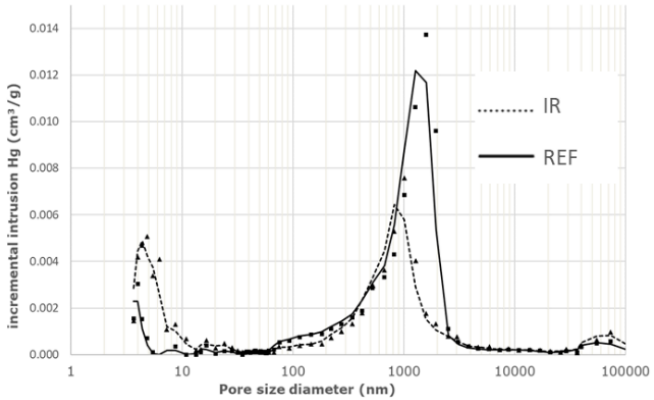

Figure 6: Pore size distribution of the irradiated samples compared to the reference samples with t_{prior}= 1 h.

Infrared spectra of the different samples did not exhibit differences as a result of irradiation. Only a small decrease in water content (3000 – 3500 cm^{-1} and from 1650 – 1655 cm^{-1}) for the irradiated samples was observed. TGA results confirm the lower water content of the irradiated samples. This is related to water radiolysis during irradiation and due to the accelerated evaporation of water by gamma heating. Moreover, in the region from 570 °C to 620 °C a small difference was observed, which is better visible for samples irradiated over a larger time span. The derivative thermo-gravimetrical curve (DTG) of a sample irradiated for 312 h at 1.25 kGy/h is shown in Figure 7. A clear difference in the range 400 °C to 650 °C is visible, related to a difference in carbonates.

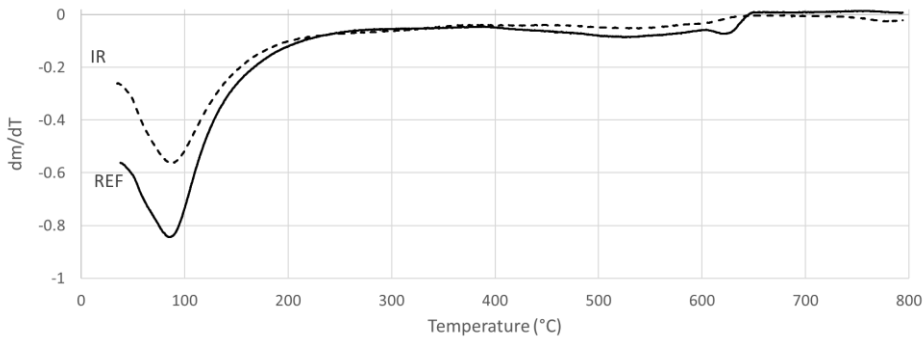

Figure 7: dm/dT curve of a 24 h cured sample prior to irradiation (dose rate: 1.25 kGy/h, total dose: 390.0 kGy) and its unirradiated reference.

Mössbauer spectroscopy was used to determine the redox ratio of ferric (Fe^{3+}) and ferrous (Fe^{2+}) iron in the irradiated and non-irradiated IP samples. Based on the relative absorption areas the $Fe^{3+}/\sum Fe$ ratio and $Fe^{2+}/\sum Fe$ ratio was calculated. An increase in Fe^{3+} content from 20 ± 5% to 39 ± 5% was observed for the 1 h cured samples prior to irradiation (Figure 8).

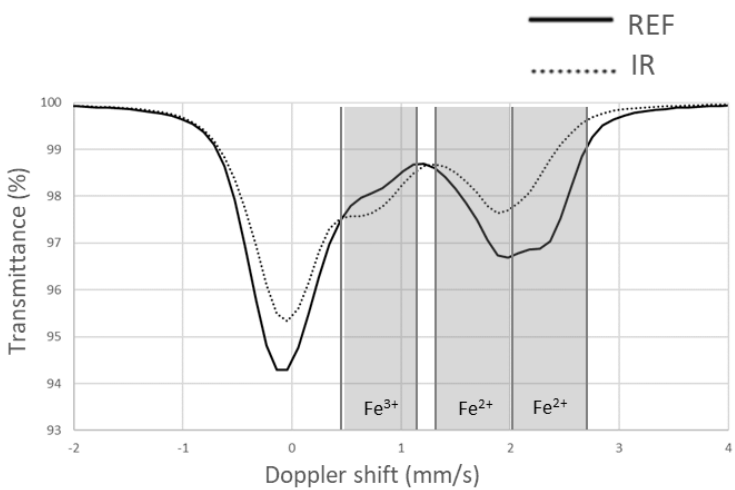

Figure 8: Comparison of the ^{57}Fe Mössbauer spectra of the irradiated and non-irradiated samples with t_{prior} = 1 h. The shaded areas indicate the regions of the higher velocity parts of the Fe^{3+} and the Fe^{2+} doublets used to fit the spectra.

Strengthening of the samples can be related to the increase in Fe^{3+} content as a result of gamma irradiation, since Fe^{3+} can take position in the silicate network [45] [46] while Fe^{2+} takes place in a trioctahedral layer [46]. Radiation-induced iron oxidation occurs as Fe^{2+} is oxidized by radiolytically produced $^{\bullet}OH$ radicals and H_2O_2. Especially in the initial reaction stage of the IP, when unbound Fe^{2+} can still be found, the effect of radiation-induced iron oxidation is expected to have the highest impact. With time, radiation-induced iron oxidation becomes more difficult as the samples dehydrate, and more Fe-atoms will already have been bound in the IP structure.

Conclusion

Alternatives to the commonly used ordinary Portland cement (OPC) matrices have been studied for radioactive waste encapsulation, in particular inorganic Polymers (IPs) and alkali activated materials (AAMs). They encompass a broad range of binder systems formed by the reaction of an alkali metal source (solid or dissolved) with a solid amorphous powdered precursor. AAMs have promising properties for the immobilization of radioactive wastes, such as high chemical and temperature resistance, low water content, absence of portlandite and low porosity. Moreover, high-density slag-based AAMs can easily be designed, offering an alternative to the high-density concretes used for gamma shielding. Due to the wide range of available precursor materials and activation solutions, tailor-made AAMs can be designed in view of specific applications. Materials can however be altered by exposure to ionizing radiation. In this study, the effect of gamma irradiation is investigated on IPs based on CaO-FexOy-SiO2 slag.

Samples cured for only 1 hour are still reactive at the start of irradiation and are therefore easily affected by gamma irradiation. As a result of gamma heating and radiolysis, water escape is promoted at the initial stage, leading to accelerated drying and accelerated (plastic) shrinkage. In this case strengthening can be associated with densification of the matrix. As water is found to be a crucial component in the radiation-induced Fe oxidation, a decrease in porosity favours this effect by preventing the escape of water from the matrix. Fe^{3+} can take position in the silicate network and contribute to the strength development of the polymer. In addition, Fe^{2+} oxidation causes densification of the matrix which

also enhances strength. Water retention moreover slows down the IP reactions, thus giving irradiation effects more time to have an impact. Multiple effects were observed for the one hour cured samples: an increase of the compressive strength by a factor of 2.20, a decrease in porosity by a factor of 0.92, and an increase of the $Fe^{3+}/\sum Fe$ ratio by a factor of 1.95. Radiation-altered carbonation was also observed.

Irradiation effects in Fe-rich IPs are complex, they occur simultaneously and moreover continuously interact. Figure 6 provides an illustration. The final response of the material depends strongly on the absorbed dose and the state of the material at the start of the irradiation.

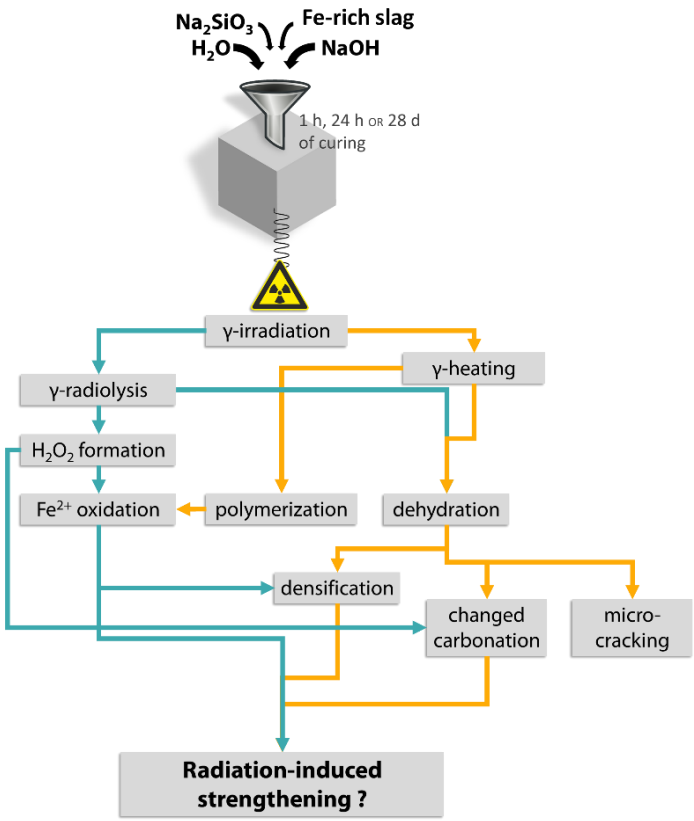

Figure 9: Radiation-induced strengthening.

The mix design used in this study should be optimized in order to focus on specific applications such as nuclear waste management.

Related work

1. B. Mast, Y. Pontikes, W. Schroeyers, B. Vandoren, and S. Schreurs, "The use of alkali activated materials in nuclear industry," in *Comprehensive Nuclear Materials*, 2nd ed., R. Konings, Ed. Elsevier Inc., 2020. [13]

2. B. Mast *et al.*, "The effect of gamma radiation on the mechanical and microstructural properties of Fe-rich inorganic polymers," *J. Nucl. Mater.*, vol. 521, 2019. [43]

3. B. Mast *et al.*, "The effect of high dose rate gamma irradiation on the curing of CaO-FexOy-SiO2 slag-based inorganic polymers: Mechanical and microstructural analysis," *J. Nucl. Mater.*, vol. in publ., 2020. [44]

4. B. Mast *et al.*, "Micromechanical and microstructural analysis of Fe-rich plasma slag-based inorganic polymers," in Cement and Concrete Composites, vol. 118, 2021. [47]

5. B. Mast., "Effects of gamma radiation on Fe-rich inorganic polymers – from microscale analysis to model design," doctoral dissertation, D/2020/2451/75. [48]

References

[1] J. L. Provis and J. S. J. Van Deventer, *Alkali-Activated Materials- State-of-the-Art Report, RILEM TC 224-AAM*, vol. 13. London: Springer, 2014.

[2] J. L. Provis, "Geopolymers and other alkali activated materials: why, how, and what?," *Mater. Struct.*, vol. 47, no. 1–2, pp. 11–25, 2014.

[3] P. Duxson, A. Fernández-Jiménez, J. L. Provis, G. C. Lukey, A. Palomo, and J. S. J. van Deventer, "Geopolymer technology: the current state of the art," *J Mater Sci*, vol. 42, pp. 2917–2933, 2007.

[4] A. Peys, C. E. White, D. Olds, H. Rahier, B. Blanpain, and Y. Pontikes, "Molecular structure of CaO – FeOx – SiO2 glassy slags and resultant inorganic polymer binders," *J. Am. Ceram. Soc.*, vol. 101, no. 12, pp. 5846–5857, 2018.

[5] J. L. Provis and J. S. J. van Deventer, Eds., *Geopolymers: structure, processing, properties and industrial applications*, 1st ed. Cambridge: Woodhead Publishing Limited, 2009.

[6] P. Krivenko, "Why alkaline activation - 60 years of the theory and practice of alkali-activated materials," *J. Ceram. Sci. Technol.*, vol. 8, no. 3, pp. 323–333, 2017.

[7] J. G. S. Van Jaarsveld, J. S. J. Van Deventer, and L. Lorenzen, "Potential use of geopolymeric materials to immobilize toxic metals: Part I. Theory and applications," *Miner. Eng.*, vol. 10, no. 7, pp. 659–669, 1997.

[8] International Atomic Energy Agency, "The Behaviours of Cementitious Materials in Long Term Storage and Disposal of Radioactive Waste: Results of a Coordinated Research Project.," Vienna, 2013.

[9] F. Chupin, A. Dannoux-papin, Y. N. Ravache, and J.-B. D'Espinose de Lacaillerie, "Water content and porosity effect on hydrogen radiolytic yields of geopolymers," *J. Nucl. Mater.*, vol. 494, pp. 138–146, 2017.

[10] J. Davidovits, "Geopolymer, Green Chemistry and Sustainable Development Solutions," in *Proceedings of the World Congress Geopolymer 2005*, 2005, p. 236.

[11] N. Vandevenne *et al.*, "Incorporating Cs and Sr into blast furnace slag inorganic polymers and their effect on matrix properties," *J. Nucl. Mater.*, vol. 503, pp. 1–12, 2018.

[12] P. Duan, C. Yan, W. Zhou, W. Luo, and C. Shen, "An investigation of the microstructure and durability of a fluidized bed fly ash–metakaolin

geopolymer after heat and acid exposure," *Mater. Des.*, vol. 74, pp. 125–137, 2015.

[13] B. Mast, Y. Pontikes, W. Schroeyers, B. Vandoren, and S. Schreurs, "The use of alkali activated materials in nuclear industry," in *Comprehensive Nuclear Materials*, 2nd ed., R. Konings, Ed. Elsevier Inc., 2020.

[14] T. Croymans-Plaghki, "Valorization of Fe-rich industrial by-products in construction materials: a radiological assessment," UHasselt, 2018.

[15] R. P. Williams and A. van Riessen, "Development of alkali activated borosilicate inorganic polymers (AABSIP)," *J. Eur. Ceram. Soc.*, vol. 31, no. 8, pp. 1513–1516, 2011.

[16] H. Takeda, S. Hashimoto, H. Matsui, S. Honda, and Y. Iwamoto, "Rapid fabrication of highly dense geopolymers using a warm press method and their ability to absorb neutron irradiation," *Constr. Build. Mater.*, vol. 50, pp. 82–86, 2014.

[17] M. G. Blackford, J. V. Hanna, K. J. Pike, E. R. Vance, and D. S. Perera, "Transmission Electron Microscopy and Nuclear Magnetic Resonance Studies of Geopolymers for Radioactive Waste Immobilization," *J. Am. Ceram. Soc.*, vol. 90, no. 4, pp. 1193–1199, 2007.

[18] J. G. Jang, S. M. Park, and H. K. Lee, "Cesium and Strontium Retentions Governed by Aluminosilicate Gel in Alkali-Activated Cements," *Materials (Basel).*, vol. 10, no. 4, pp. 1–13, 2017.

[19] J. L. Provis, P., A. Walls, and J. S. J. Van Deventer, "Geopolymerisation kinetics. 3. Effects of Cs and Sr salts," *Chem. Eng. Sci.*, vol. 63, no. 18, pp. 4480–4489, 2008.

[20] Z. Aly *et al.*, "Aqueous leachability of metakaolin-based geopolymers with molar ratios of Si / Al = 1. 5 – 4," *J. Nucl. Mater.*, vol. 378, no. 2, pp. 172–179, 2008.

[21] D. D. Dimas, I. P. Giannopoulou, and D. Panias, "Utilization of Alumina Red Mud for Synthesis of Inorganic Polymeric Materials," *Miner. Process. Extr. Metall. Rev.*, vol. 30, no. 3, pp. 211–239, 2009.

[22] H. Xu and J. S. J. Van Deventer, “The geopolymerisation of alumino-silicate minerals,” *Int. J. Miner. Process.*, vol. 59, no. 3, pp. 247–266, 2000.

[23] C. Dupuy, A. Gharzouni, I. Sobrados, N. Texier-mandoki, X. Bourbon, and S. Rossignol, “Thermal resistance of argillite based alkali-activated materials. Part: Identification of the formed crystalline phases,” *Mater. Chem. Phys.*, vol. 218, no. May, pp. 262–271, 2018.

[24] A. Fernández-Jiménez, J. Y. Pastor, A. Martin, and A. Palomo, “High-Temperature Resistance in Alkali-Activated Cement,” *J. Am. Ceram. Soc.*, vol. 93, no. 10, pp. 3411–3417, 2010.

[25] W. Xuequan, Y. Sheng, S. Xiadong, and T. Mingshu, “Alkali-activated slag cement based radioactive waste forms,” *Cem. Concr. Res.*, vol. 21, no. 2, pp. 16–20, 1991.

[26] J. G. Jang, S. M. Park, and H. K. Lee, “Physical barrier effect of geopolymeric waste form on diffusivity of cesium and strontium,” *J. Hazard. Mater.*, vol. 318, pp. 339–346, 2016.

[27] G. Qian, D. D. Sun, and J. H. Tay, “New aluminium-rich alkali slag matrix with clay minerals for immobilizing simulated radioactive Sr and Cs waste,” *J. Nucl. Mater.*, vol. 299, no. 3, pp. 199–204, 2001.

[28] M. Y. Khalil and E. Merz, “Immobilization of intermediate-level wastes in geopolymers,” *J. Nucl. Mater.*, vol. 211, no. 2, pp. 141–148, 1994.

[29] C. Kuenzel *et al.*, “Encapsulation of Cs/Sr contaminated clinoptilolite in geopolymers produced from metakaolin,” *J. Nucl. Mater.*, vol. 466, pp. 94–99, Nov. 2015.

[30] S. Xiaodong, Y. Sheng, W. Xuequan, and T. Mingshu, “Immobilization of Simulated High-Level Wastes into Waste Form,” *Cem. Concr. Res.*, vol. 24, no. 1, pp. 133–138, 1994.

[31] S. Goñi, A. Guerrero, and M. P. Lorenzo, “Efficiency of fly ash belite cement and zeolite matrices for immobilizing cesium,” *J. Hazard. Mater.*, vol. 137, no. 3, pp. 1608–1617, 2006.

[32] C. Shi and A. Fernández-Jiménez, “Stabilization/solidification of hazardous and radioactive wastes with alkali-activated cements,” *J. Hazard. Mater.*, vol. 137, no. 3, pp. 1656–1663, 2006.

[33] C. Chlique, D. Lambertin, P. Antonucci, F. Frizon, and P. Deniard, “XRD Analysis of the Role of Cesium in Sodium-Based Geopolymer,” *J. Am. Ceram. Soc.*, vol. 98, no. 4, pp. 1308–1313, 2015.

[34] X. Peng, Y. Xu, Z. Xu, D. Wu, and D. Li, “Effect of simulated radionuclide strontium on geopolymerization process,” *procedia Environ. Sci.*, vol. 31, pp. 325–329, 2016.

[35] Z. Xu *et al.*, “Immobilization of strontium-loaded zeolite A by metakaolin based- geopolymer,” *Ceram. Int.*, vol. 43, no. 5, pp. 4434–4439, 2017.

[36] Q. Guangren, L. Yuxiang, Y. Facheng, and S. Rongming, “Improvement of metakaolin on radioactive Sr and Cs immobilization of alkali-activated slag matrix,” *J. Hazard. Mater.*, vol. 92, no. 3, pp. 289–300, 2002.

[37] D. Chartier, B. Muzeau, L. Stefan, J. Sanchez-canet, and C. Monguillon, “Magnesium alloys and graphite wastes encapsulated in cementitious materials: Reduction of galvanic corrosion using alkali hydroxide activated blast furnace slag,” *J. Hazard. Mater.*, vol. 326, pp. 197–210, 2017.

[38] A. Rooses, D. Lambertin, D. Chartier, and F. Frizon, “Galvanic corrosion of Mg-Zr fuel cladding and steel immobilized in Portland cement and geopolymer at early ages,” *J. Nucl. Mater.*, vol. 435, no. 1–3, pp. 137–140, 2013.

[39] A. Rooses, P. Steins, A. Dannoux-Papin, D. Lambertin, A. Poulesquen, and F. Frizon, “Encapsulation of Mg-Zr alloy in metakaolin-based geopolymer,” *Appl. Clay Sci.*, vol. 73, no. 1, pp. 86–92, 2013.

[40] L. Machiels, L. Arnout, P. Yan, P. Tom Jones, B. Blanpain, and Y. Pontikes, “Transforming Enhanced Landfill Mining Derived Gasification / Vitrification Glass into Low-Carbon Inorganic Polymer Binders and Building Products,” *J. Sustain. Metall.*, vol. 3, no. 2, pp. 405–415, 2016.

[41] European Comittee for standardization, “EN 196-6:2010 - Methods of testing cement - Part 6: Determination of fineness,” pp. 1–18, 2010.

[42] P. Douvalis, A. Polymeros, and T. Bakas, “IMSG09: A 57Fe -119Sn Mössbauer spectra computer fitting program with novel interactive user interface,” *J. Phys. Conf. Ser.*, vol. 217, no. 1, 2010.

[43] B. Mast *et al.*, “The effect of gamma radiation on the mechanical and microstructural properties of Fe-rich inorganic polymers,” *J. Nucl. Mater.*, vol. 521, 2019.

[44] B. Mast *et al.*, “The effect of high dose rate gamma irradiation on the curing of CaO-FeOx-SiO2 slag based inorganic polymers: Mechanical and microstructural analysis,” *J. Nucl. Mater.*, vol. 539, 2020.

[45] P. N. Lemougna, K. J. D. Mackenzie, G. N. L. Jameson, and H. R. U. F. Chinje, “The role of iron in the formation of inorganic polymers (geopolymer) from volcanic ash: a 57Fe Mössbauer spectroscopy study,” *J. Mater. Sci.*, vol. 48, pp. 5280–5286, 2013.

[46] A. Peys, A. P. Douvalis, V. Hallet, H. Rahier, B. Blanpain, and Y. Pontikes, “Inorganic Polymers from CaO-FeOx-SiO2 Slag: The Start of Oxidation of Fe and the Formation of a Mixed Valence Binder,” *Front. Mater.*, vol. 6, no. 212, pp. 1–10, 2019.

[47] B. Mast *et al.*, “Micromechanical and microstructural analysis of Fe-rich plasma slag-based inorganic polymers,” in Cement and Concrete Composites, vol. 118, 2021.

[48] B. Mast., “Effects of gamma radiation on Fe-rich inorganic polymers – from microscale analysis to model design,” doctoral dissertation, D/2020/2451/75.

-

Hoofdredacteur Mr. Michel Sonck Rédacteur en chef